JOURNAL OF THERMOPHYSICS AND HEAT TRANSFER
Vol. 19, No. 1, January–March 2005

Heat Transfer Prediction of Rotating Rectangular Channels Using Reynolds Stress Model

Mohammad Al-Qahtani*
King Fahd University of Petroleum and Minerals, Dhahran 31261, Saudi Arabia
and
Hamn-Ching Chen† and Je-Chin Han‡
Texas A&M University, College Station, Texas 77843

Computations were performed to study three-dimensional turbulent flow and heat transfer in a rotating smooth rectangular channel with channel aspect ratio of 4:1. Two channel orientations ($\beta = 90$ and 135 deg from the rotation direction) were investigated, focusing on the high-rotation and high-density-ratio effects on the heat-transfer characteristics of the 135-deg orientation. The rotation number and inlet coolant-to-wall density ratios, $\Delta\rho/\rho$, were varied from 0.0 to 0.28 and from 0.122 to 0.40, respectively; the Reynolds number was fixed at 10^4. The effect of rotation and coolant-to-wall density ratio on the fluid flow and heat transfer characteristics is reported. The study shows considerable spanwise heat transfer differences across the leading and trailing surfaces. Also, it indicates complete flow reversal in the leading part of the channel, altering heat-transfer characteristics. The numerical results are compared with the experimental data for both stationary and rotating rectangular channels.

Nomenclature

C_f	=	friction coefficient, $\tau_o/(0.5\rho W_b^2)$
C_{fo}	=	friction coefficient in fully developed turbulent nonrotating tube flow
D_h, D	=	hydraulic diameter, m
h	=	heat transfer coefficient, W/m^2 K
k	=	thermal conductivity of coolant, W/m K
Nu	=	local Nusselt number, hD/k
Nu_o	=	Nusselt number in fullydeveloped turbulent nonrotating tube flow, hD/k
Pr	=	Prandtl number, $\mu C_p/k$
Re	=	Reynolds number, $\rho W_b D_h/\mu$
Ro	=	rotation number, $\Omega D_h/W_b$
R_r	=	radius from axis of rotation
S	=	streamwise distance, m
T	=	local coolant temperature, °C
T_o	=	coolant temperature at inlet, °C
T_w	=	wall temperature, °C
W_b	=	bulk velocity in streamwise direction, m/s
β	=	angle of channel orientation measured from direction of rotation
$\Delta\rho/\rho$	=	inlet coolant-to-wall density ratio, $(T_w - T_o)/T_w$
θ	=	dimensionless temperature, $(T - T_o)/(T_w - T_o)$
μ	=	dynamic viscosity of coolant, N s/m^2
ρ	=	density of coolant, kg/m^3
ρ_o	=	density of coolant at inlet, kg/m^3
τ_o	=	shear stress at the wall, N/m^2
Ω	=	rotational speed, rad/s

Received 27 December 2003; revision received 9 May 2004; accepted for publication 10 May 2004.

*Assistant Professor, Department of Mechanical Engineering; mqahtani@kfupm.edu.sa.
†Professor, Ocean Engineering Program, Department of Civil Engineering. Senior Member AIAA.
‡Professor, Turbine Heat Transfer Laboratory, Department of Mechanical Engineering. Associate Fellow AIAA.

Introduction

Motivation

TO improve thermal efficiency, gas-turbine stages are being designed to operate at increasingly high inlet temperatures. A widely used method for cooling turbine blades is to bleed lower-temperature gas from the compressor and circulate it within and around each blade. The coolant typically flows through a series of straight ducts connected by 180-deg bends and roughened with ribs or pin fins to enhance heat transfer.

With the advancement of gas-turbine technology, it has become necessary to focus attention on regions exposed to the most severe conditions. One of these regions is the trailing edge of a turbine blade. Due to significant shortage of cooling space for internal cooling, it is becoming one of the most important problems for by gas-turbine designers. Because the profile of a turbine blade is curved and gets thinner toward the trailing edge, this leads to two effects on cooling channels. The cooling channels' cross section becomes rectangular and their orientation changes from normal to an angle with the direction of rotation. This thinning and change of the channel orientation alter the effective secondary-flow pattern from that of a square duct. For this reason, one cannot simply apply the knowledge of the rotationally induced flow pattern in a square channel, which is normal to the rotation direction, to that of a rectangular channel, which is at an angle to the rotation direction. Therefore, an investigation of a rectangular channel that is oriented at an angle to the rotational direction is necessary to further understand the heat-transfer characteristics of the internal cooling channels in a gas-turbine blade.

Literature Review

Extensive experimental studies have been performed to study the heat-transfer characteristics in smooth channels. Wagner et al.[1,2] investigated the effects of buoyancy and Coriolis forces on heat transfer in square passages with outward and inward flow. Soong et al.[3] and Murata and Mochizuki[4] studied the secondary-flow effects due to rotation by considering smooth-walled rectangular ducts with different aspect ratios ranging from 0.2 to 5.0. They concluded that the aspect ratio is a critical parameter. Parsons et al.[5] studied the effect of model orientation and wall-heating condition on heat transfer in a rotating two-pass square channel. Dutta and Han[6] considered the effects of orientation and rotation on heat transfer in

three channel orientations. They found that a change in the channel orientation about the rotating frame causes a change in the secondary-flow structure and the associated flow and turbulence distribution. Willett and Bergles[7] performed a detailed investigation of the heat transfer in a narrow, 10:1 smooth rectangular channel oriented at 60 deg to the r–z plane. Most of their focus dealt with exploring the contribution of buoyancy forces under rotation. They found that the duct orientation induced a significant variation in the heat-transfer coefficient in the spanwise direction. It was also found that the normalized Nusselt number at the far aft end of the trailing side (or the bottom equivalent in this paper) is a strong function of rotation number and buoyancy number. In subsequent work, Willett and Bergles[8] studied the same channel experimentally but with orientation 90 deg from the direction of rotation. They found that the trailing and leading-side heat-transfer coefficients increase and decrease, respectively, with the buoyancy number.

In addition to the experimental studies mentioned above, several studies have been conducted to predict numerically the flow and heat transfer in radially rotating smooth ducts. Iacovides and Launder,[9] Prakash and Zerkle,[10] Dutta et al.,[11] and Bo et al.[12] studied one-passage smooth ducts with normal channel orientation from the direction of rotation, that is, $\beta = 90$ deg. Sathyamurthy et al.,[13] Stephens et al.,[14] Iacovides et al.,[15] and Bonhoff et al.,[16] reported numerical predictions for rotating smooth two-passage ducts with $\beta = 90$ deg. The differential Reynolds stress model with wall function in FLUENT code was used in the calculation of Bonhoff et al.[16]

J. C. Han and co-workers have performed parallel experimental and numerical studies on heat transfer in rectangular rotating channels with different aspect ratios (AR)[17–20] Azad et al.[17] studied the effect of the channel angle orientation ($\beta = 90$ deg and $\beta = 135$ deg from the direction of rotation) on two-pass rectangular (aspect ratio 2:1) smooth and ribbed channels. Al-Qahtani et al.[18] studied numerically the rotating smooth case in Azad et al.[17] They reported the effect of Coriolis and buoyancy forces on secondary flow. Heat-transfer coefficient prediction was compared with the experimental data of Azad et al.[17] for both normal and twisted channel orientations. It predicted fairly well the complex three-dimensional flow and heat-transfer characteristics resulting from a sharp 180° turn, rotation, centrifugal buoyancy forces, and channel orientation. They also investigated the effect of the rotation number Ro and inlet coolant-to-wall density ratio $\Delta\rho/\rho$. On the same line, Griffith et al.[19] studied experimentally the effect of channel orientation on rotating smooth and ribbed rectangular channels with channel aspect ratio of 4:1. They investigated a broad range of flow parameters including Reynolds number ($Re = 5 \times 10^3$–40×10^3), rotation number ($Ro = 0.04$–0.3), and coolant-to-wall density ratio ($\Delta\rho/\rho = 0.122$). Al-Qahtani et al.[20] studied numerically the ribbed configuration of Griffith et al.[19] and compared the results with their experimental data. The smooth channel configuration of Griffith et al.[19] will be studied numerically in the present study. The primary objective of this study is to apply advanced computational fluid dynamics methods for practical channel configurations close to engine conditions in order to facilitate solid physical understanding of flow physics. More specifically, it is intended to 1) predict the three-dimensional flow and heat transfer for rotating smooth one-pass rectangular ducts (AR = 4:1) with two channel orientations ($\beta = 135$ deg and 90 deg) and compare the results with the experimental data of Griffith et al.[19] and 2) investigate the effect of high rotation and high density ratios on the secondary flow, streamwise velocity, and temperature fields in the 135 deg orientation channel and to find whether it is significant enough to require consideration in designing the cooling channels at the trailing edge of a turbine blade.

Description of Problem

Figure 1A shows the two-channel orientations that are studied: $\beta = 90$ deg, corresponding to the midportion of a turbine blade,

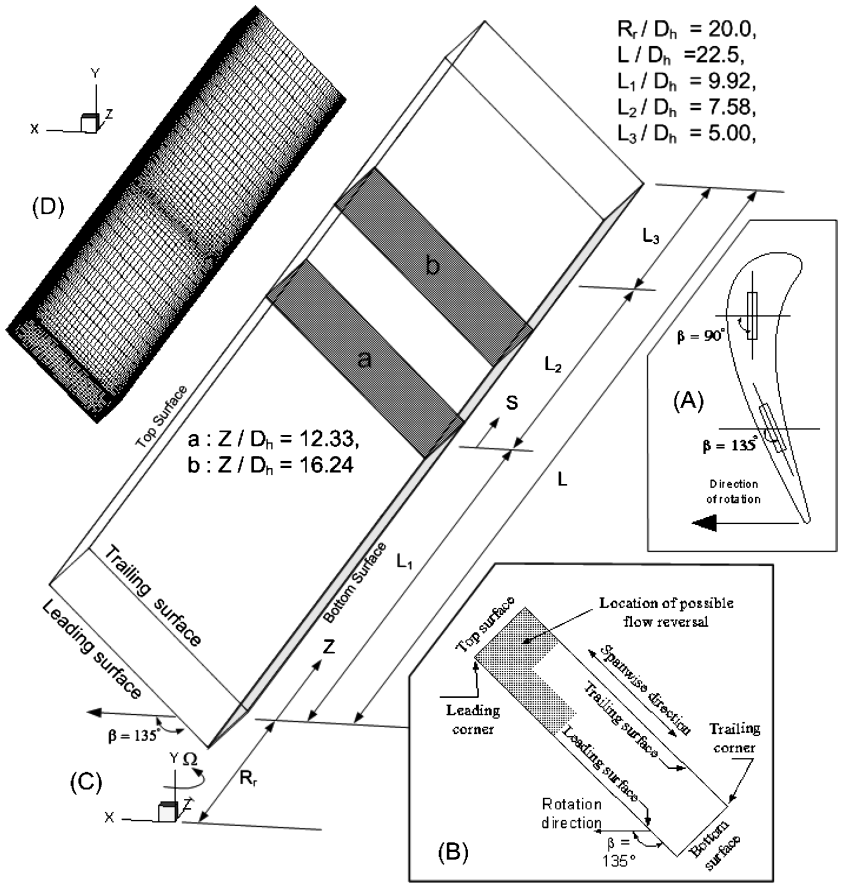

Fig. 1 Rectangular channel with aspect ratio (AR) 4:1: A, Channel orientation; B, illustrative lablels; C, geometry; and D, computational grid.

Table 1 Summary of cases studied, $Re = 10 \times 10^3$

Case	Ro	$\Delta\rho/\rho$	β	Validation with experiment
1	0.00	0.12	——	Yes
2	0.14	0.12	90 deg	Yes
3	0.14	0.12	135 deg	Yes
4	0.28	0.12	135 deg	NA
5	0.28	0.20	135 deg	NA
6	0.28	0.40	135 deg	NA

and $\beta = 135$ deg, corresponding to the serpentine passages in the trailing edge region of a blade. The channel has a rectangular cross section with channel aspect ratio of 4:1. Figure 1B explains the nomenclature of the cross section. Two of the four side walls, in the rotational direction, are denoted as the leading and trailing surfaces, respectively, whereas the other two side walls are denoted as the top and bottom surfaces. The corner between the leading and top surfaces is designated as the leading corner and the corner between the trailing and bottom surfaces is designated as the trailing corner. The channel hydraulic diameter, D_h, is 2.0 cm. The lengths of the channel are shown in Fig. 1C. The distance from the inlet of the channel to the axis of rotation (Y axis) is given by $R_r/D_h = 20.0$ and the length of the channel is given as $L/D_h = 22.5$. The channel consists of an unheated starting length ($L_1/D_h = 9.92$), a heated section ($L_2/D_h = 7.58$) corresponding to the test section in Griffith et al.,[19] and an unheated exit section ($L_3/D_h = 5.00$). The arc length S is measured from the beginning of the heated section to its end. The two axial locations at which results are presented are at locations a ($Z/D_h = 12.33$) and b ($Z/D_h = 16.24$). A summary of the cases studied is given in Table 1.

Computational Procedure

Overview

The Reynolds-averaged Navier–Stokes (RANS) equations, in conjunction with a near-wall Reynolds stress turbulence model are solved using the chimera RANS method of Chen et al.[21,22] The governing equations with the second-moment closure turbulence model were described in detail by Chen et al.[21,22] and will not be repeated here. The flow is considered to be incompressible because the Mach number is quite low. However, the density in the centrifugal force terms is approximated by $\rho = \rho_o T_o/T$ to account for the density variations caused by the temperature differences, where ρ_o and T_o, are the density and temperature at the inlet. In general, the density is also a function of rotation speed because the centrifugal force creates a pressure gradient along the duct. As mentioned by Al-Qahtani et al.,[20] the maximum pressure variation between the channel inlet and exit in Griffith et al.[19] was approximately 0.0113 atm for the highest rotation number considered in the present study, 0.28 (i.e., $\Omega = 550$ rpm). This gives a maximum density variation of only about 1.1% from the inlet to the outlet of the duct at the highest rotation number. It is therefore reasonable to omit the density variation caused by the pressure gradients induced by the channel rotation. For completeness, the numerical method will be briefly summarized in the following section.

Chimera RANS Method

The present method solves the mean flow and turbulence quantities in arbitrary combinations of embedded, overlapped, or matched grids using a chimera domain-decomposition approach. In this approach, the solution domain was first decomposed into a number of smaller blocks to facilitate efficient adaptation of different block geometries, flow solvers, and boundary conditions for calculations involving complex configurations and flow conditions. Within each computational block, the finite-analytic numerical method of Chen et al.[23] was employed to solve the unsteady RANS equations on a general curvilinear, body-fitted coordinate system. The coupling between the pressure and velocity was accomplished using the hybrid PISO/SIMPLER algorithm of Chen and Patel.[24] The method satisfied continuity of mass by requiring the contravariant velocities to have a vanishing divergence at each time step. Pressure was solved by using the concept of pseudovelocities, which, when combined with the finite-analytic discretization, gives the Poisson equation for pressure. To ensure the proper conservation of mass and momentum between the linking grid blocks, the grid-interface conservation techniques of Chen and Chen[25] were employed to eliminate the unphysical mass source resulting from the interpolation errors between the chimera grid blocks. In the present study, the numerical grids in the block-overlap region are fully matched. Therefore, grid-interface conservation is automatically satisfied.

Boundary Conditions

At the inlet of the duct ($Z = 0$), a uniform velocity profile was used for the W-component. For the U, V-components, all Reynolds stresses and energy dissipation were assumed to be zero. It should be mentioned that the unheated starting length (L_1) is long enough for the velocity profile and Reynolds stresses to assume the values of fully developed turbulent conditions before reaching the heated section, which is our region of interest in the present study. At the exit of the duct, zero-gradient boundary conditions were assumed for the mean velocities and all turbulent quantities, whereas linear extrapolation was used for the pressure field. Physically this implies that a) diffusion is neglected at the exit and b) the near-exit-cell values of all variables are convected in or out at the exit boundary. Use of this treatment decouples the computational domain from the outside. When the buoyancy effects are small, the flow leaves the computational domain everywhere at the exit boundary, where the conditions are essentially parabolic (i.e., zero gradient). Hence, for such cases, the outflow treatment is reasonable. When buoyancy effects are significant, however, small reverse radial flows may occur near the top surface, implying some entrainment of the fluid at the exit boundary. Under these conditions, the use of zero-gradient treatment at the exit is not satisfactory. To fix this situation, the computational domain was extended to include an unheated exit length so that the exit was far removed from the region of interest, thus making acceptable use of the zero-gradient exit-boundary treatment. The coolant fluid at the inlet of the duct is air at uniform temperature $T = T_o$ (i.e., $\theta = (T - T_o)/(T_w - T_o) = 0$). The wall temperature of the unheated sections is kept constant at $T = T_o$ ($\theta = 0$), whereas the wall temperature of the heated section is kept constant at $T = T_w$ ($\theta = 1$).

Computational Grid Details

Figure 1D shows the computational grid for the smooth duct. The grid was elliptically generated using an interactive grid generation code, GRIDGEN.[26] It was then divided into three overlapped chimera grid blocks to facilitate the implementation of the near-wall turbulence model and the specification of the boundary conditions. To provide adequate resolution of the viscous sublayer and buffer layer adjacent to a solid surface, the minimum grid spacing in the near-wall region is maintained at 10^{-3} of the hydraulic diameter, which corresponds to a wall coordinate y^+ on the order of 0.5. The number of grid points in the streamwise direction from inlet to outlet is 50, whereas in the cross-stream plane it is 33×75. The grid was made dense at the beginning of the heated section in order to provide accurate resolution of the thermal-boundary-layer development. The number of grid points and their distributions in the present smooth duct were obtained on the basis of extensive grid-refinement studies performed in Chen et al.[21,22] and Al-Qahtani et al.[18] for similar smooth channels of square and rectangular cross sections. Therefore, it is believed that the present grid will produce nearly grid-independent results with accurate resolution of the boundary-layer profile and Nusselt-number distribution. In all calculations, the rms and maximum absolute errors for both the mean flow and turbulence quantities were monitored for each computational block to ensure complete convergence of the numerical solutions and a convergence criterion of 10^{-5} was used for the maximum rms error.

Results and Discussion

As summarized in Table 1, computations were performed for one Reynolds number (10^4), rotation numbers ranging from 0 to 0.28,

and inlet coolant-to-wall density ratios $\Delta\rho/\rho$ ranging from 0.122 to 0.40, with two channel orientations of $\beta = 90$ deg and 135 deg. The Nusselt numbers presented here were normalized with a smooth tube correlation by Dittus–Boelter/McAdams (Rohsenow and Choi[27]) for fully developed turbulent nonrotating tube flow,

$$Nu_o = 0.023 Re^{0.8} Pr^{0.4}$$

whereas the friction coefficients were normalized with a smooth tube correlation[28] for fully developed turbulent flow:

$$C_{\text{fo}} = 0.078 Re^{-0.25}$$

Velocity and Temperature Fields

Figures 2–4 show the calculated secondary-flow vectors and constant-temperature contours at two axial stations for various rotation numbers and coolant-to-wall density ratios, as mentioned in Table 1. Note that the axial stations at which the results are presented are viewed from upstream of the channel. For the stationary case, Fig. 2a shows that secondary corner vortices are generated as a result of the Reynolds stress anisotropy. It can be noticed from the corresponding temperature-contour plots that the cooler fluid is located in the core region of the channel cross section. For the rotating 90-deg case, Fig. 2b shows that the Coriolis forces produce a cross-stream two-vortex flow structure that pushes the cold fluid from the core toward the trailing surface and then brings it back along the top and bottom surfaces to the leading surface. This results in a small temperature gradient near the leading surface (hence lower heat-transfer coefficients) and a steeper one near the trailing surface (hence higher heat-transfer coefficients), as seen from the corresponding temperature contour plot of Fig. 2b. Moreover, the cooler, heavier fluid near the trailing surface will be accelerated by the centrifugal buoyancy force, whereas the hotter, lighter fluid near the leading surface will be decelerated to maintain the continuity in the streamwise direction.

Figure 3 shows the calculated secondary-flow vectors and constant temperature contours for cases 3 and 4. It can be seen from Fig. 3a ($Ro = 0.14$ and $\Delta\rho/\rho = 0.122$) that the Coriolis force in the 135-deg configuration produces a secondary flow that pushes the cold fluid away from the corner of the leading and top surfaces. This produces two elongated counterrotating vortices near the trailing and leading surfaces. These vortices become stronger as the rotation number is increased to 0.28 (Fig. 3b). As a result of this secondary flow, the cold fluid is pushed toward the bottom surface. This is because the Coriolis force is from the leading to the trailing corner, which in turn gives rise to an opposite pressure gradient, which drives the near-wall fluid along the leading and trailing sides from the bottom to the top walls. From there, the fluid moves back along the channel core to the bottom surface. This can be seen from the corresponding temperature-contour plots, in which high-temperature contours are located near the leading corner, whereas cold fluid is located near the bottom surface.

Figure 4 shows the calculated secondary flow vectors and constant temperature contours for cases 5 and 6. As the density ratio is increased to 0.20 (Fig. 4a), the vortex near the leading surface is pushed toward the bottom surface. Downstream of the channel, the vortex near the trailing surface grows at the expense of the one near the leading surface. Moreover, the cold fluid is pushed more toward the bottom surface. Increasing the density ratio further to 0.40 (Fig. 4b), results in pushing the two counterrotating vortices further toward the bottom surface with strong mixing. The temperature contours indicate that the hot fluid extends more toward the center of the channel. In general, the temperature contours in the preceding figures indicate that the hot fluid is located next to the top surface and the upper half of the leading surface. This is an important result, as it explains the occurrence of flow reversal in these regions for some cases in the coming figures. Another consequence is that the temperature gradient will be small in the vicinity of the top corner (hence lower heat-transfer coefficients) and steep in the vicinity of the bottom corner (hence higher heat-transfer coefficients), as seen from the corresponding contour plot.

Figure 5 shows velocity vectors (plotted every other vector) and temperature contours midway between the leading and trailing surfaces for various rotation numbers and density ratios. The unheated sections were removed to focus on the heated section. Figure 5a shows the streamwise velocity and temperature contours for $Ro = 0.00$ and $\Delta\rho/\rho = 0.122$ (case 1). This case will be used as a baseline to which the other figures will be compared. Under stationary conditions, typical channel flow can be seen in this figure. The temperature distribution is symmetric between the top and bottom surfaces. The heated regions are confined to near the top and bottom surfaces.

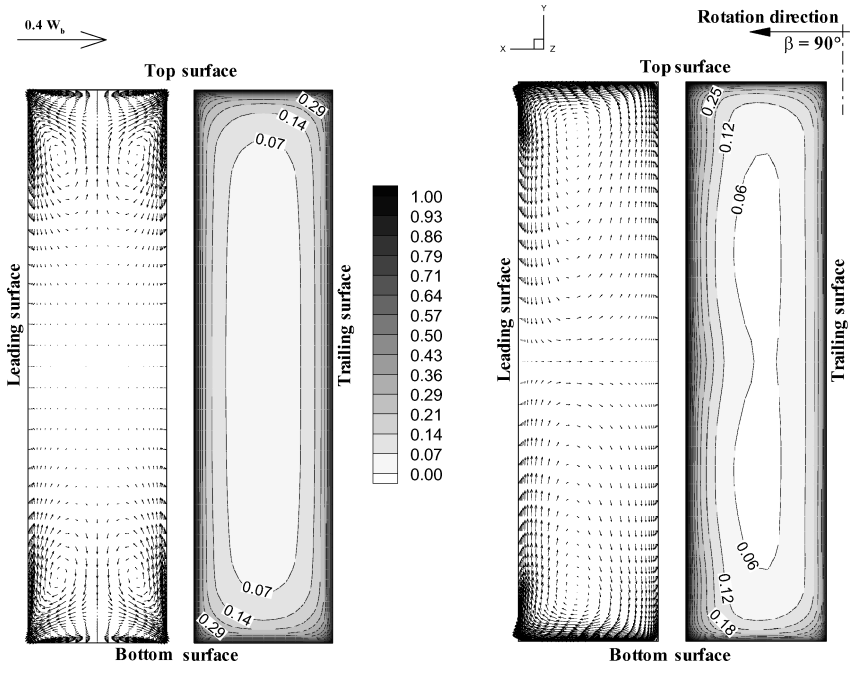

Fig. 2 Secondary flows and dimensionless temperature $[\theta = (T - T_o)/(T_w - T_o)]$ at axial location $Z/D_h = 16.24$, $\beta = 90$ deg: a) $Ro = 0.00$, $\Delta\rho/\rho = 0.12$ and b) $Ro = 0.14$, $\Delta\rho/\rho = 0.12$.

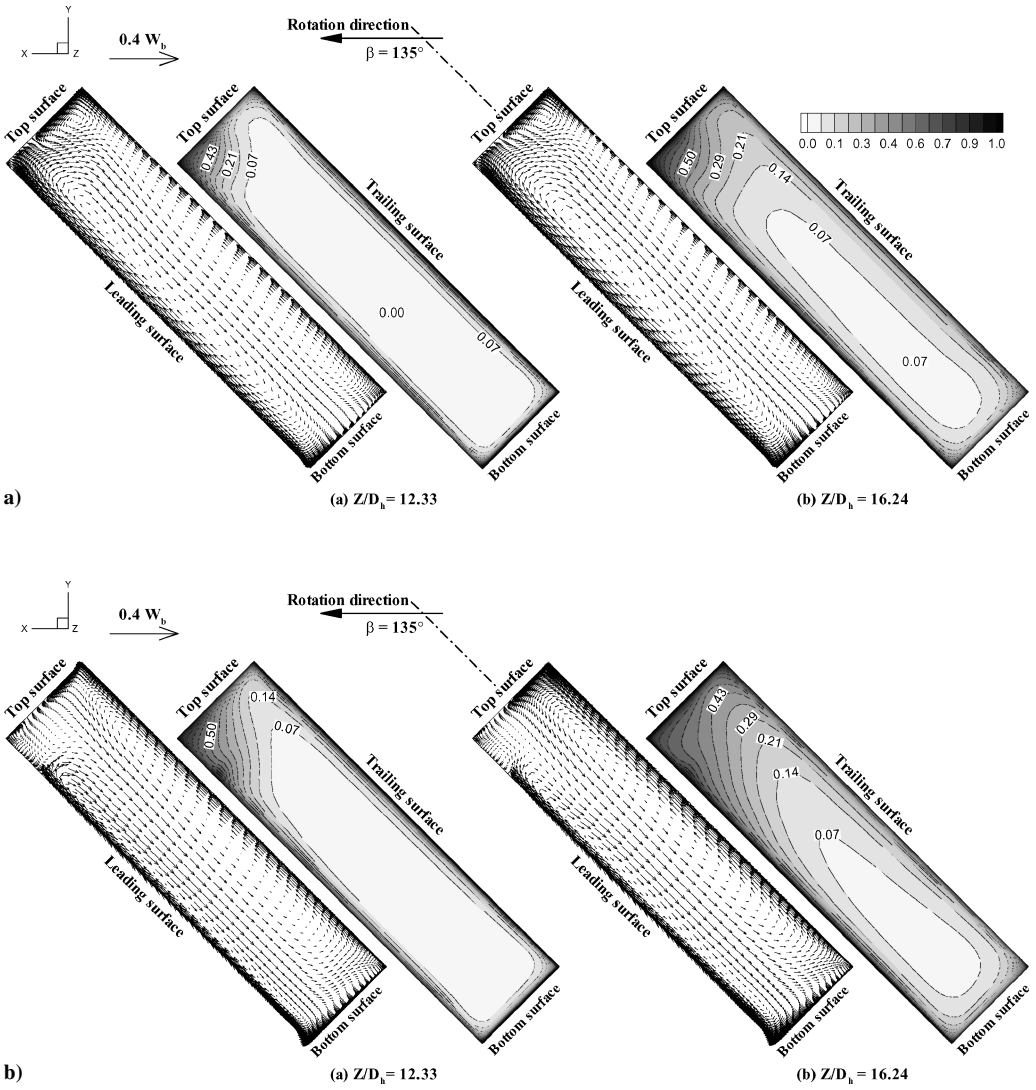

Fig. 3 Secondary flows and dimensionless temperature $[\theta=(T-T_o)/(T_w-T_o)]$ for $\beta=135$ deg: a) $Ro=0.14$, $\Delta\rho/\rho=0.122$ and b) $Ro=0.28$, $\Delta\rho/\rho=0.122$.

Downstream of the heated section, the hot regions extend slightly toward the channel core. Under low rotation number ($Ro=0.14$, case 3), Fig. 5b shows that the hot region near the top surface extends more toward the channel core, especially downstream of the channel. The velocity profile becomes thicker near the top surface due to buoyancy effects, but no flow reversal occurs in this low-rotation low-density ratio case. As the rotation number is increased further to 0.28 (case 4), Fig. 5c shows that the fluid temperature near the top surface increases more in value and in extent. At this location, the velocity distribution is thicker and it is on the verge of velocity reversal, as seen from the nearly zero-gradient velocity profile near the top surface. In Fig. 5d, the rotation number is fixed at $Ro=0.28$, and the density ratio is increased to 0.20 (case 5). Flow reversal occurs near the top surface in this case. It extends a considerable distance upstream of the heated section end. But it is limited (in the spanwise direction) to $0.7D_h$ from the top surface. Increasing the density ratio more to 0.40 (Fig. 5e, case 6) causes the reverse flow to be stronger.

To facilitate our understanding of the flow-reversal effect on the Nusselt-number-ratio and friction-coefficient behavior, a detailed examination of the velocity distribution for the high-rotation high-density case (case 6) is given in Figs. 6 and 7. Figure 6 shows the velocity vectors at three planes parallel to the leading/trailing surfaces. Planes a and c are $0.03D_h$ from the leading and trailing surfaces, respectively, whereas plane c is midway between the leading and trailing surfaces. Near the trailing surface (Fig. 6a), the flow reversal extends in the spanwise direction to only $0.5D_h$ from the top surface. Moving further to midway between the leading and trailing surfaces (Fig. 6b), the flow reversal extends further (in the spanwise direction) to $0.80D_h$ from the top surface. Near the leading surface (Fig. 6c), the flow reversal extends to $1.15D_h$ in the spanwise direction.

Figure 7 shows the streamwise velocity distribution at five planes parallel to the top/bottom surfaces. The planes are arranged on the basis of an increasing distance from the bottom surface. Plane a is $0.10D_h$ from the bottom surface, whereas plane b is midway between the top and bottom surfaces. Planes c, d, and e are $0.63D_h$, $0.33D_h$, and $0.10D_h$ from the top surface, respectively. Near the bottom surface (Fig. 7a), no flow reversal occurs as expected, because cold fluid is available there. Moving away from the bottom surface and exactly at the center of the spanwise distance, Fig. 7b shows that the velocity profile experiences retardation next to the leading surface, whereas it is accelerated more near the trailing surface. Moving further toward the top surface (Fig. 7c), strong flow reversal near the leading surface is observed. It increases in strength (Fig. 7d) to the extent that it reaches the trailing surface downstream of the heated section. Very near to the top surface (Fig. 7e), complete flow reversal occurs. This important finding

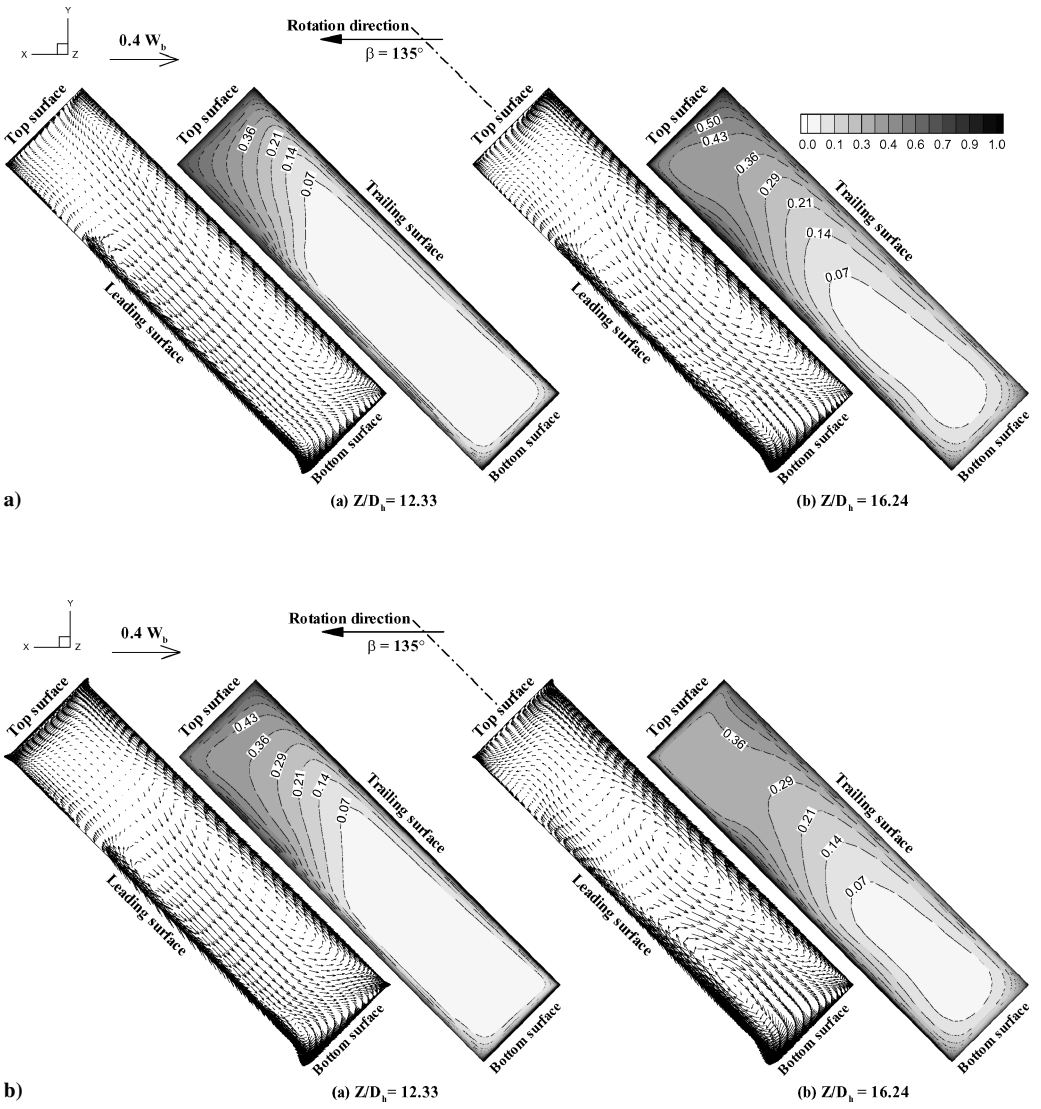

Fig. 4 Secondary flows and dimensionless temperature [$\theta = (T-T_o)/(T_w-T_o)$], for $\beta = 135$ deg: a) $Ro = 0.28$, $\Delta\rho/\rho = 0.2$ and b) $Ro = 0.28$, $\Delta\rho/\rho = 0.40$.

explains why the leading Nusselt number increases downstream of the heated section. This is due to flow reversal, where cooler fluid from the downstream unheated section is convected over the heated section.

Rotational Buoyancy and Flow Reversal

From the previous figures, it is clear that the cold fluid is pushed toward the bottom surface by the Coriolis-force-induced secondary flow, whereas the hot fluid is located near the top surface and the top part of the leading surface. Thus, the cooler, heavier fluid near the bottom surface will be accelerated by the centrifugal buoyancy force, whereas the hotter, lighter fluid near the top surface and top part of the leading surface will be decelerated to maintain continuity in the streamwise direction. Thus, if there is a flow reversal, it should take place on surfaces near the leading corner. This is what happens with high-rotation and high-density cases where flow reversal take place near the top surface and the upper part of the leading surface (Figs. 5c and 5d). This is one of the differences between the 135- and 90-deg-oriented rotating channels. In the normal channels ($\beta = 90$ deg), if flow reversal should occur, it would occur only on the middle part of the leading surface, as was shown by Al-Qahtani et al.[18]

Reynolds Stresses

Figure 8 shows the calculated Reynolds stress components for $Ro = 0.00$ and 0.14 (case 1) at axial location $Z/D_h = 13.80$. Because there is no rotation, Fig. 8 shows a symmetric distribution of the normal stress components with respect to the channel bisectors. The turbulence intensity level of the $\sqrt{(\overline{uu})}/W_b$ component is high near the top and bottom surfaces (about 7%) and diminishes gradually toward the core region of the channel. The turbulence intensity level of the $\sqrt{(\overline{vv})}/W_b$ and $\sqrt{(\overline{ww})}/W_b$ components is rather high near all surfaces (7% and 13%, respectively) and decreases toward the duct center. In addition, a rather high degree of anisotropy close to the leading/trailing surfaces is observed ($3 \leq \overline{ww}/\overline{vv} \leq 6$ or $3 \leq \overline{ww}/\overline{uu} \leq 16$).

For the high-rotation high-density case (case 6), Fig. 9 shows a dramatic change in the pattern of Reynolds stresses. This is clearly caused by the Coriolis-force-driven cross-stream flow in the presence of two strong counterrotating vortices. The high $\sqrt{(\overline{uu})}/W_b$ components near the top and bottom surfaces in the stationary case have been convected to the trailing surface with a turbulence intensity level of 9%. Relatively high levels of turbulence intensity (8% to 14%) arise near the trailing corner and the trailing surface, whereas lower values (5% to 10%) were observed in the channel core. Also, a high degree of anisotropy on the trailing

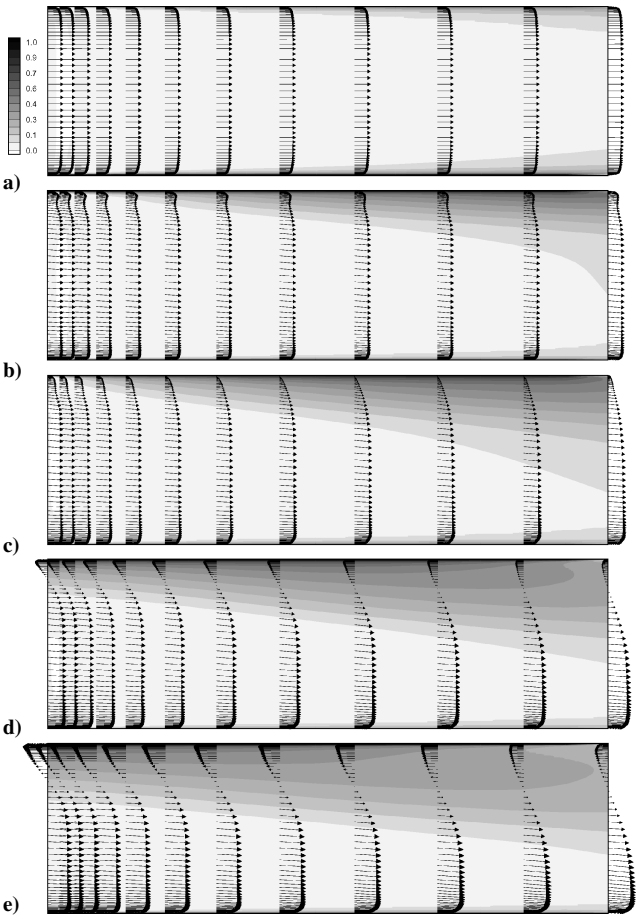

Fig. 5 Velocity vectors (plotted every other vector) and temperature contours midway between leading and trailing surfaces, for $\beta = 135$ deg: a) $Ro = 0.0$, $\Delta\rho/\rho = 0.12$; b) $Ro = 0.14$, $\Delta\rho/\rho = 0.12$; c) $Ro = 0.28$, $\Delta\rho/\rho = 0.12$; d) $Ro = 0.28$, $\Delta\rho/\rho = 0.20$; and e) $Ro = 0.28$, $\Delta\rho/\rho = 0.40$.

surface ($4.2 \leq \overline{ww}/\overline{uu}$ or $\overline{ww}/\overline{vv} \leq 5.0$) and on the leading surface ($5.8 \leq \overline{ww}/\overline{uu}$ or $\overline{ww}/\overline{vv} \leq 2.8$) was observed.

Detailed Local Heat-Transfer-Coefficient Distribution

For various rotation numbers and density ratios, Figs. 10 and 11 show the local Nusselt-number-ratio contours of the leading and trailing surfaces, respectively. The unheated sections were cut to focus on the heated section. The nonrotating case (case 1) in Fig. 10a (Fig. 11a for the trailing surface) will be used as a baseline for comparison and discussion. Figures 10b–10e (Figs. 11b–11e for the trailing surface) are for $\beta = 135$ deg, whereas Fig. 10f (Fig. 11f for the trailing surface) is for $\beta = 90$ deg.

Effect of Increasing the Rotation Number on the Leading Surface

Figure 10a shows the Nusselt-number-ratio contour plots on the leading surface for the nonrotating case (case 1). The Nusselt-number ratios near the beginning of the heated section are high due to the thinner boundary layers. Downstream, they decrease and asymptotically approach the fully developed value. In Fig. 10b (case 3), the rotation number is increased to 0.14, whereas the density ratio is kept fixed at 0.12. We notice significant Nusselt-number-ratio variation in the spanwise direction. Next to the bottom surface, the Nusselt-number ratios are as high as 1.3 times the corresponding Nusselt-number-ratios in the stationary case; then they decrease toward the top surface. The reason for this has been explained in the velocity section, where it was mentioned that part of the cold fluid comes back from the bottom surface along the leading surface. This means that heat transfer will be high at the bottom part of the leading surface and then decrease toward the top surface. When

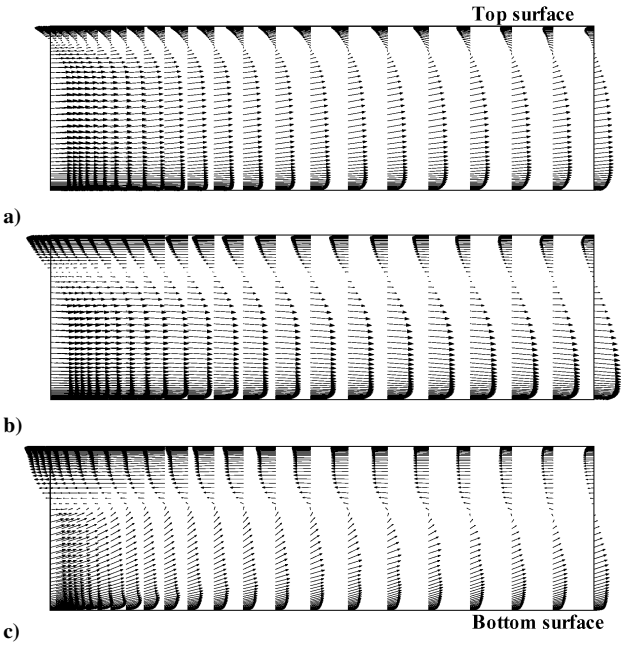

Fig. 6 Velocity vectors for $Ro = 0.28$, $\Delta\rho/\rho = 0.40$, and $\beta = 135$ deg: a) $0.03D_h$ from the trailing surface; b) midway between leading and trailing surfaces; and c) $0.58D_h$ from the leading surface.

the rotation number was increased to 0.28 (Fig. 10c, case 4), the Nusselt-number ratios next to the bottom surface increased further, to as high as 1.6 times the corresponding Nusselt-number ratios in the stationary case. Then they decreased toward the top surface, reaching values 40% lower than in the corresponding stationary case.

Effect of Increasing the Density Ratio on the Leading Surface

In Fig. 10d (case 5), the rotation number is kept fixed at 0.28 and the density ratio is increased to 0.20. This figure shows that the high-Nusselt-number-ratio regions next to the bottom surface increase further to 1.9 times the corresponding Nusselt-number ratios in the stationary case. At the end of the heated section, a small region of high Nusselt-number ratios next to the top surface occurs due to flow reversal, which takes place on the leading surface as seen in Figs. 6 and 7. Increasing the density ratio further to 0.40 (Fig. 10e, case 6) causes the Nusselt-number ratios (next to the bottom surface) to be as high as 2.6 times the corresponding stationary Nusselt-number ratios. It is also seen from this figure that the high Nusselt-number ratios downstream and next to the top surface extend more due to increase in the flow-reversal strength, as was discussed in detail when dealing with Figs. 6 and 7.

Effect of Increasing the Rotation Number on the Trailing Surface

Figure 11a shows the Nusselt-number-ratio contour plots on the trailing surface for the nonrotating case (case 1). It is identical to Nusselt-number ratios in Fig. 10a as they should be. In Fig. 11b (case 3), the rotation number is increased to 0.14, whereas the density ratio is kept fixed at 0.12. Again we notice significant Nusselt-number-ratio variation in the spanwise direction but with a structure different from that of the leading surface. Next to the bottom surface, the Nusselt-number ratios are as high as 1.6 times the corresponding Nusselt-number ratios in the stationary case. In the middle of the trailing surface, a large region of high Nusselt-number ratios is surrounded by a region of higher Nusselt-number ratios. Near the top surface, the Nusselt-number ratios are the same as in the stationary case. When the rotation number was increased to 0.28 (Fig. 11c, case 4), the Nusselt-number ratios next to the bottom surface increased further, to as high as 1.9 times the corresponding Nusselt-number ratios in the stationary case. Then they decrease

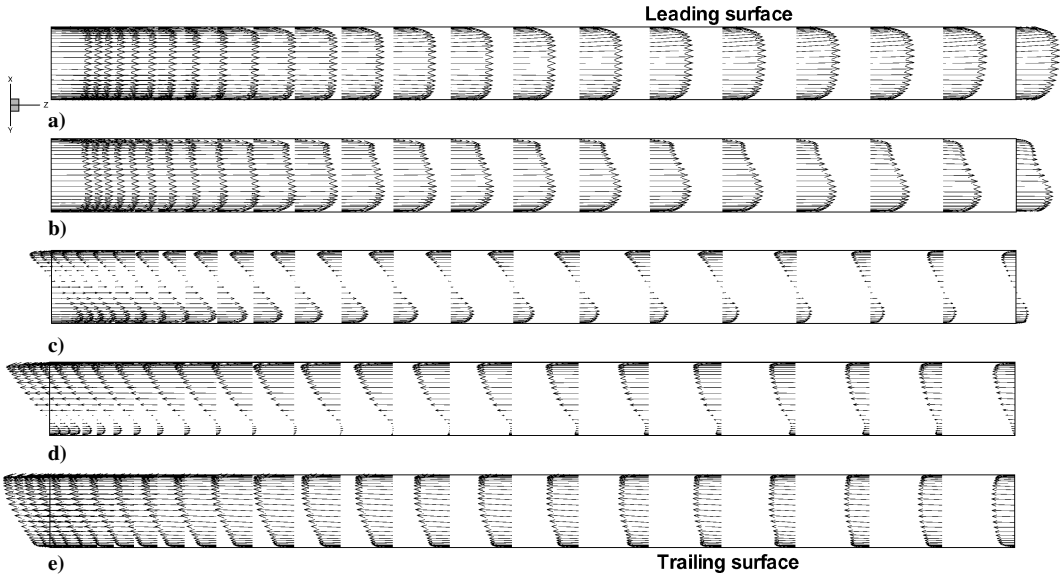

Fig. 7 Velocity vectors for $Ro = 0.28$, $\Delta\rho/\rho = 0.40$, and $\beta = 135$ deg: a) $0.10D_h$ from the bottom surface; b) midway between top and bottom surfaces; c) $0.63D_h$ from the top surface; d) $0.33D_h$ from the top surface; and e) $0.10D_h$ from the top surface.

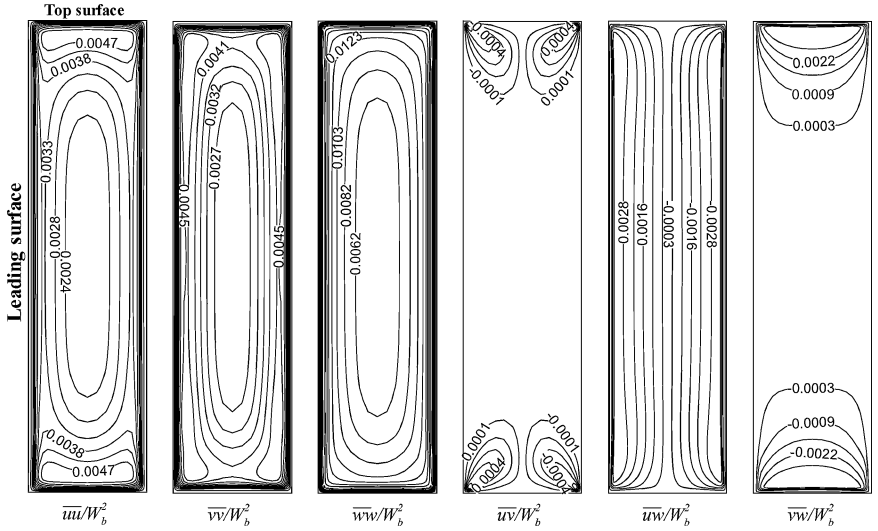

Fig. 8 Reynolds-stress components for nonrotating channel at axial location $Z/D_h = 13.80$, $\Delta\rho/\rho = 0.12$.

toward the top surface, reaching values equivalent to those in the corresponding stationary case.

Effect of Increasing the Density Ratio on the Trailing Surface

In Fig. 11d (case 5), the rotation number is kept fixed at 0.28 and the density ratio is increased to 0.20. It is seen in this figure that the high-Nusselt-number regions next to the bottom surface increase further, to as high as 2.3 times the corresponding Nusselt-number ratios in the stationary case. Then they decrease toward the top surface, reaching values equal to those in the corresponding stationary case. Increasing the density ratio further to 0.40 (Fig. 11e, case 6) causes the Nusselt-number ratios (next to the bottom surface) to be as high as 2.6 times the corresponding stationary Nusselt-number ratios. At the end of the heated section, a small region of high Nusselt-number ratios next to the top surface is generated due to flow reversal as was discussed in Figs. 6 and 7.

Effect of Channel Orientation on the Leading and Trailing Surfaces

For fixed rotation number and density ratio ($Ro = 0.14$ and $\Delta\rho/\rho = 0.122$), Figs. 10b and 10f show the Nusselt-number-ratio contours on the leading side for $\beta = 135$ deg and 90 deg (cases 3 and 2), respectively. When these figures are compared with the nonrotating leading side (Fig. 10a, case 1), the Nusselt-number ratios decreased in the 90-deg case by 18%, but remained almost the same for the135-deg case. Figures 11b and 11f show the Nusselt-number-ratio contours on the trailing side for $\beta = 135$ deg and 90 deg (cases 3 and 2), respectively. When these figures are compared with the nonrotating trailing side (Fig. 11a, case 1), the Nusselt-number ratios increased by 22% and 19% for the 90- and 135-deg cases, respectively.

Spanwise Averaged Heat-Transfer Coefficients

Figure 12 shows the effect of the rotation number and inlet coolant-to-wall density ratio on the Nusselt-number-ratio distributions for several rotation numbers and coolant-to-wall density ratios. The Reynolds number is fixed at 10^4. The leading Nusselt-number ratios decrease at the entry of the heated section with an increase in the rotation number and the density ratio. However, downstream and beyond the middle of the heated section, the Nusselt-number ratios begin to increase with an increase in the rotation-number and density

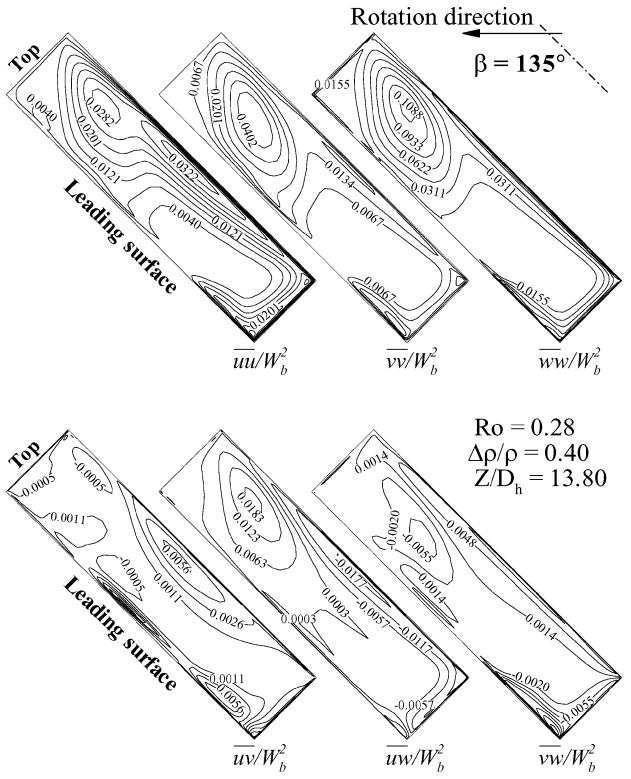

Fig. 9 Reynolds stress components at axial location $Z/D_h = 13.80$, $Ro = 0.28$, and $\Delta\rho/\rho = 0.40$.

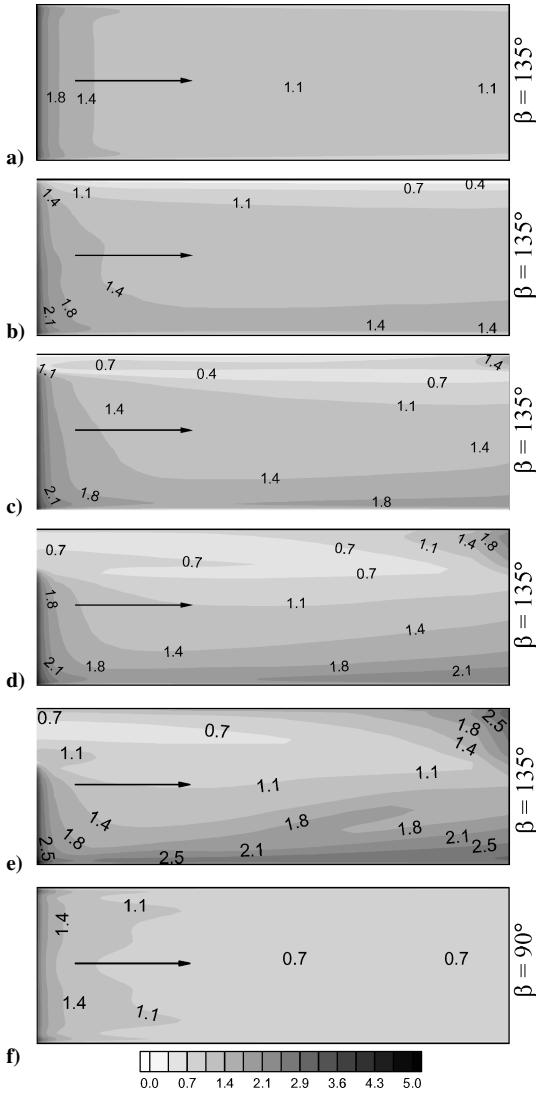

Fig. 10 Detailed Nusselt number distribution on leading surface: a) $Ro = 0.0$, $\Delta\rho/\rho = 0.12$; b) $Ro = 0.14$, $\Delta\rho/\rho = 0.12$; c) $Ro = 0.28$, $\Delta\rho/\rho = 0.12$; d) $Ro = 0.28$, $\Delta\rho/\rho = 0.20$; e) $Ro = 0.28$, $\Delta\rho/\rho = 0.40$; and f) $Ro = 0.14$, $\Delta\rho/\rho = 0.12$

ratios. In their experimental study, Griffith et al.[19] attributed this increase in the leading-surface Nusselt-number to the overall better mixing provided by the Coriolis force. The present study confirms this explanation and shows that the increase in the Nusselt-number ratios is due to the strong flow reversals that take place downstream, next to the upper part of the leading surface, as explained in the discussion of Figs. 6 and 7.

Figure 12 also shows that the trailing- and bottom-surface Nusselt numbers increase with an increase in the rotation number and density ratio. The bottom surface exhibits the highest heat-transfer enhancement of all of the surfaces in the duct. This is attributed to the fact that this surface is the primary recipient of the Coriolis-induced secondary flow. This phenomenon was illustrated in the discussion of the secondary flow in Figs. 3 and 5 in the Velocity section. In those figures, the Coriolis-induced cross-stream cold flow that impinges on the bottom surface and the trailing corner and thus increases heat transfer.

The top-surface Nusselt number exhibits the lowest heat-transfer coefficient of all of the surfaces in the duct. This is attributed to the fact that this surface is mainly receiving the hot fluid coming back from the bottom surface along the trailing and leading surfaces. The top-surface Nusselt-number ratios decrease as the rotation number is increased from 0.00 to 0.28 (with fixed density ratio of 0.12). However, as the density ratio is increased from 0.12 to 0.40 (with the rotation number fixed at 0.28), the trend of the top-surface Nusselt-number ratios reverses. It becomes low at the beginning of the heated section and increases asymptotically toward the channel downstream. This behavior, which was also noticed by Dutta and Han,[6] Prakash and Zerkle,[10] and Al-Qahtani et al.,[18] is a direct consequence of the streamwise strong velocity reversal that occurs on the whole face of the top surface (see Figs. 6 and 7). This flow reversal is due to the rotational buoyancy that opposes the flow near the top surface. As a result of this, the turbulence level and hence the heat transfer increase on this surface.

In Fig. 13, the spanwise-averaged Nusselt number ratios (Nu/Nu_o) as compared made with the experimental data of Griffith et al.[19] To compare the effects of the channel orientation on the heat transfer, Fig. 13 shows the Nusselt-number ratios for the three smooth cases: 1, 2, and 3. In this figure, the inlet coolant-to-wall density ratio was held constant at value of 0.122. The effect of the model orientation can be seen by comparing the 135-deg Nusselt-number ratios with the 90-deg ones. It can be seen that the 135-deg Nusselt-number ratios are a) higher on the leading surface and lower on the trailing surface and b) lower on the top surface and higher on the bottom surface. The reason behind this could be explained in the light of Figs. 3 and 4, where it can be seen that the cold fluid received by the 135-deg leading surface is cooler than that received by the 90-deg leading surface. This is because, in the 90-deg case, the cold fluid reaches the leading surface after it passes over the trailing surface and both of the two side surfaces. However, in the 135-deg case, the cold fluid moves directly to the bottom surface, at which it splits and comes back along the leading surface, which means higher heat transfer than in the 90-deg case. For the trailing surface, all of the cold fluid (in the 90-deg case) moves directly to the trailing surface, after which it splits at its middle.

On the other hand, the cold fluid in the 135-deg case moves first to the bottom surface, at which only part of it will come back to the trailing surface, which means less heat transfer than in the 90-deg case. It can be noted that the Nusselt-number ratios of the top surface of the 135-deg rotating case are lower than those corresponding to the 90-deg rotating case. This is attributed to the fact that in the 135-deg case, most of the top surface behaves as a leading surface,

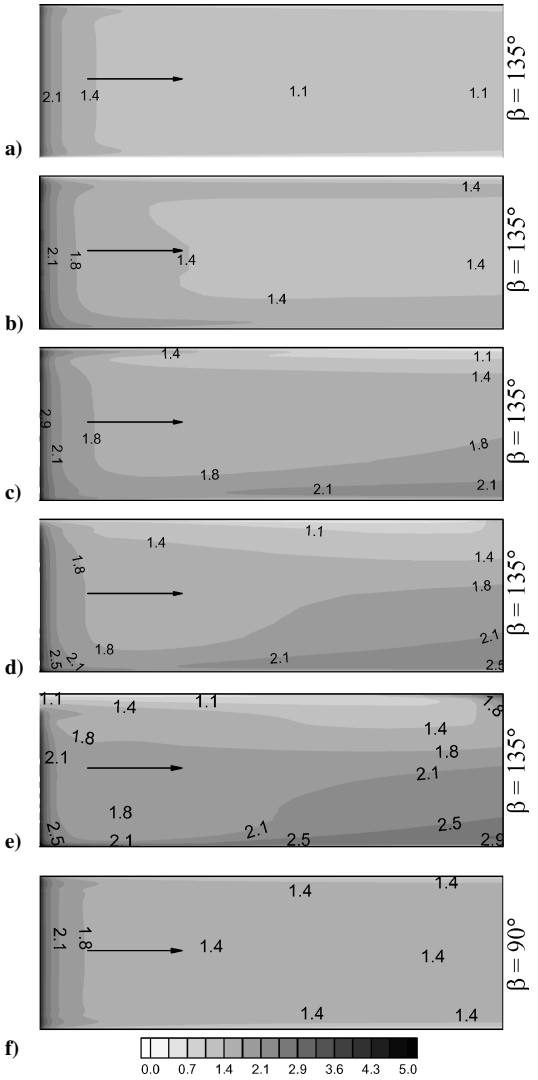

Fig. 11 Detailed Nusselt number distribution on trailing surface: a) $Ro = 0.0$, $\Delta\rho/\rho = 0.12$; b) $Ro = 0.14$, $\Delta\rho/\rho = 0.12$; c) $Ro = 0.28$, $\Delta\rho/\rho = 0.12$; d) $Ro = 0.28$, $\Delta\rho/\rho = 0.20$; e) $Ro = 0.28$, $\Delta\rho/\rho = 0.40$; and f) $Ro = 0.14$, $\Delta\rho/\rho = 0.12$.

in the sense that the cold fluid is moving away from this surface. Similarly, it can be noticed that the Nusselt-number ratios of the bottom surface of the 135-deg case are higher than those corresponding to the 90-deg case. This is because the bottom surface in this case behaves as a trailing surface in the sense that it receives the cold fluid directly from the duct core.

Comparisons with the experimental values reveal that, for the nonrotating case, the match between experiment and prediction is good on all surfaces. For the rotating case, fair agreement on the leading, top, and bottom sides is achieved for $\beta = 90$ and 135 deg, but with underprediction on the trailing surface for both cases. The reasons behind this difference could be any of the following: 1) It is known that agreement with smooth surface data is hard to obtain because any surface imperfection on the copper plates will increase the heat-transfer data compared to the computational results. 2) The uncertainty in the experimental data was found to be 25% for $Re = 10^4$. 3) The predicted Nusselt-number ratios are based on a uniform wall-temperature boundary condition, whereas the experimental ones are based on a uniform wall-heat-flux boundary condition.

Spanwise Averaged Friction-Coefficient Ratios

Figure 14 shows the effect of rotation number and inlet coolant-to-wall density ratio on the friction-coefficient-ratio distribution for the 135-deg configuration. The unheated starting and exit sections are not shown. The rotation number was varied from 0 to 0.28 and the inlet-density ratio ($\Delta\rho/\rho$) was varied from 0.12 to 0.40. For the nonrotating case (case 1), the friction-factor ratios on all the surfaces maintain the fully developed value, as seen from the solid line. An increase in the rotation number and density ratio increases friction coefficients greatly on the leading, trailing, and bottom surfaces. The bottom surface exhibits the highest friction-coefficient increase of all of the surfaces in the duct. These higher friction coefficients (especially on the bottom surface) are caused by the Coriolis force pushing the high-momentum fluid toward the bottom surface, which creates a thinner boundary layer. On the other hand, as the density ratio is increased, the top-surface friction coefficient increases greatly instead of decreasing. The initial decrease is due to the velocity distribution becoming thicker in cases 3 and 4 (see Fig. 5). The subsequent increase in the friction coefficient (case 5 and 6) is attributed to the centrifugal-buoyancy-induced reversed flow destabilizing the near-wall turbulent boundary layer, as shown in Fig. 5.

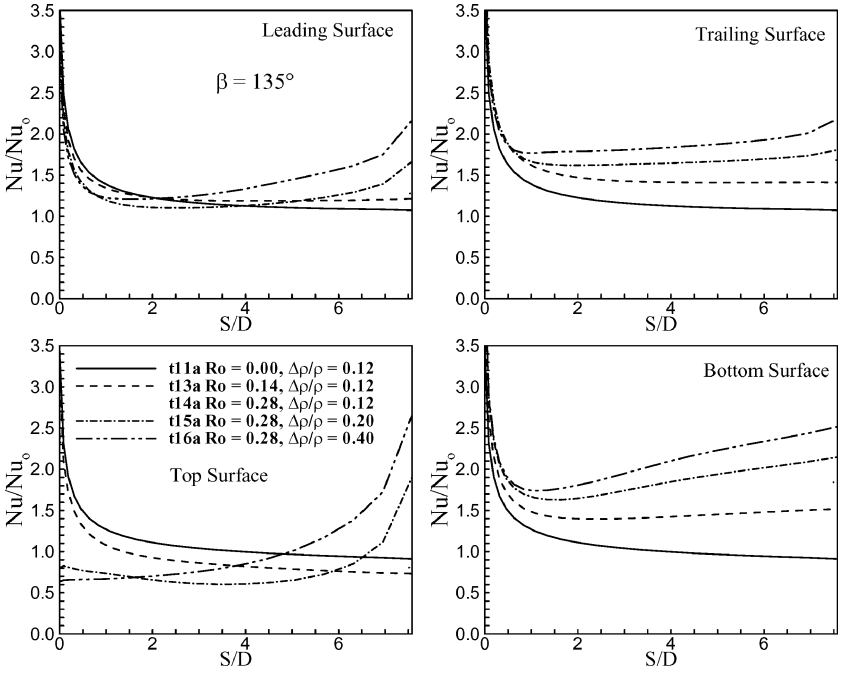

Fig. 12 Effect of the rotation number and coolant-to-wall density ratio on Nusselt-number ratios: $\beta = 135$ deg, $Ro = 10^4$.

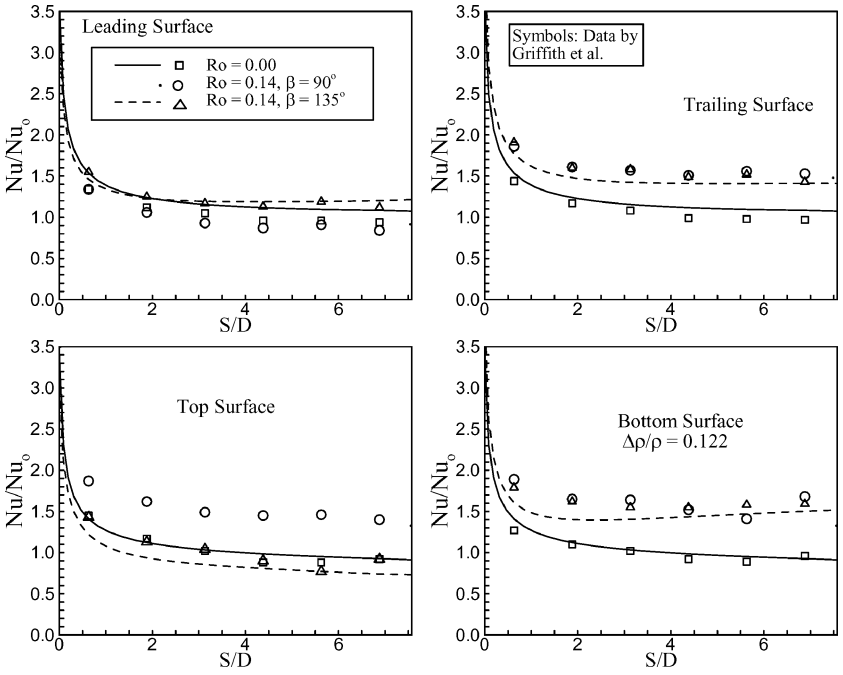

Fig. 13 Effect of rotation and channel angle on Nusselt-number distribution for smooth duct, $Re = 10 \times 10^3$.

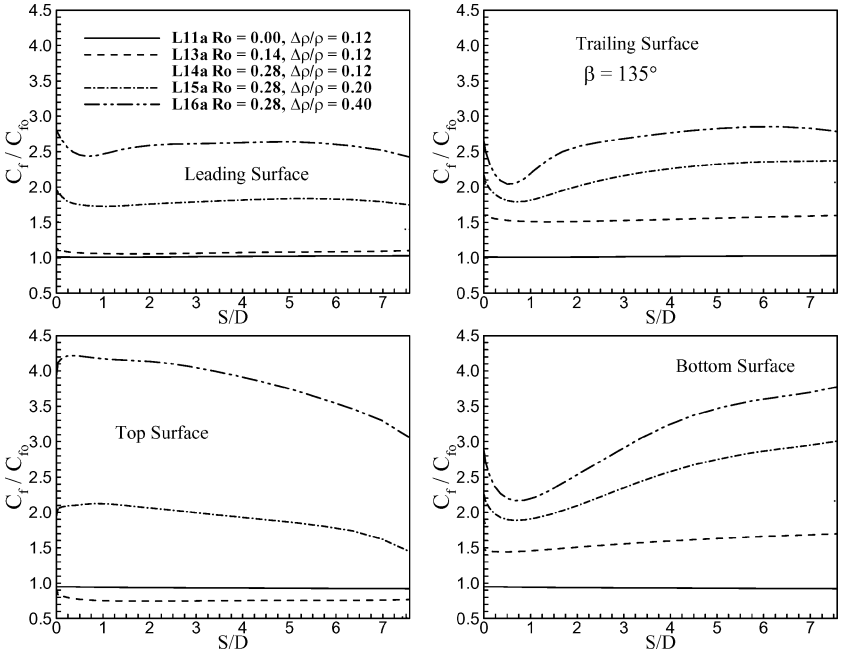

Fig. 14 Effect of the rotation and coolant-to-wall density ratio on friction coefficient ratios: $\beta = 135$ deg, $Ro = 10 \times 10^3$.

Conclusions

A multiblock RANS method was employed to predict three-dimensional flow and heat transfer in a rotating smooth rectangular channel with an aspect ratio of 4:1 and for various rotation numbers and inlet coolant-to-wall density ratios. The channel is oriented at 90 and 135 deg from the direction of rotation. A near-wall second-moment closure model was used to predict the complex three-dimensional flow and heat-transfer characteristics resulting from the large aspect ratio, rotation, centrifugal buoyancy forces, and channel orientation. The main findings of the study may be summarized as follows:

1) The Coriolis force induces secondary flow that pushes cold fluid from the channel core to the bottom surface via two counterrotating vortices. This is desirable because the bottom surface is closer to the trailing edge of the turbine blade, and thus is likely to experience a higher external heat flux than the top surface.

2) Flow reversal occurs next to the top surface and the top portion of the leading surface due to rotational buoyancy effects. This dramatically alters the Nusselt number and the friction coefficient on these surfaces.

3) Spanwise heat-transfer differences exist across the leading and trailing surfaces. This observation should be taken into account when the cooling channels of a gas-turbine blade are designed.

4) The Nusselt-number ratios and friction coefficient show a strong dependence on rotation number and density ratio.

Acknowledgments

The leading author, Mohammad Al-Qahtani, received financial support from King Fahd University, Saudi Arabia, to complete this

paper. The computations were performed on the Cray J90 at the Texas A&M Supercomputer Center under a supercomputer research grant. This support is very much appreciated.

References

[1]Wagner, J. H., Johnson, B. V., and Hajek, T. J., "Heat Transfer in Rotating Passages with Smooth Walls and Radial Outward Flow," American Society of Mechanical Engineers, ASME Paper 89-GT-272, 1989.

[2]Wagner, J. H., Johnson, B. V., and Kopper, F. C., "Heat Transfer in Rotating Serpentine Passage with Smooth Walls," *Journal of Turbomachinery*, Vol. 113, No. 3, 1991, pp. 321–330.

[3]Soong, C. Y., Lin, S. T., and Hwang, G. J., "An Experimental Study of Convective Heat Transfer in Radially Rotating Rectangular Ducts," *Journal of Heat Transfer*, Vol. 113, Aug. 1991, pp. 604–611.

[4]Murata, A., and Mochizuki, S., "Effect of Cross-Sectional Aspect Ratio on Turbulent Heat Transfer in an Orthogonally Rotating Rectangular Smooth Duct," *International Journal of Heat and Mass Transfer*, Vol. 42, No. 20, 1999, pp. 3803–3814.

[5]Parsons, J. A., Han, J. C., and Zhang, Y. M., "Effects of Model Orientation and Wall Heating Condition on Local Heat Transfer in a Rotating Two-Pass Square Channel with Rib Turbulators," *International Journal of Heat and Mass Transfer*, Vol. 38, No. 7, 1995, pp. 1151–1159.

[6]Dutta, S., and Han, J. C., "Local Heat Transfer in Rotating Smooth and Ribbed Two-Pass Square Channels with Three Channel Orientations," *Journal of Heat Transfer*, Vol. 118, No. 3, 1996, pp. 578–584.

[7]Willett, F. T., and Bergles, A. E., "Heat Transfer in Rotating Narrow Rectangular Ducts with Heated Sides Oriented at 60° to the *R–Z* Plane," *Journal of Turbomachinery*, Vol. 123, No. 2, 2001, pp. 288–295.

[8]Willett, F. T., and Bergles, A. E., "Heat Transfer in Rotating Narrow Rectangular Ducts with Heated Sides Parallel to the *R–Z* Plane," *Journal of Heat Transfer*, Vol. 124, No. 1, 2002, pp. 1–7.

[9]Iacovides, H., and Launder, B. E., "Parametric and Numerical Study of Fully Developed Flow and Heat Transfer in Rotating Rectangular Ducts," *Journal of Turbomachinery*, Vol. 113, July 1991, pp. 331–338.

[10]Prakash, C., and Zerkle, R., "Prediction of Turbulent Flow and Heat Transfer in a Radially Rotating Square Duct," *Journal of Turbomachinery*, Vol. 114, No. 4, 1992, pp. 835–846.

[11]Dutta, S., Andrews, M. J., and Han, J. C., "Prediction of Turbulent Heat Transfer in Rotating Smooth Square Ducts," *International Journal of Heat and Mass Transfer*, Vol. 39, No. 12, 1996, pp. 2505–2514.

[12]Bo, T., Iacovides, H., and Launder, B. E., "Developing Buoyancy-Modified Turbulent Flow in Ducts Rotating in Orthogonal Mode," *Journal of Turbomachinery*, Vol. 117, No. 3, 1995, pp. 474–484.

[13]Sathyamurthy, P. S., Karki, K. C., and Patankar, S. V., "Prediction of Turbulent Flow and Heat Transfer in a Rotating Square Duct with a 180 Deg. Bend," American Society of Mechanical Engineers, ASME Paper 94-GT-197, June 1994.

[14]Lin, Y.-L., Shih, T. I.-P., Stephens, M. A., and Chu, M. K., "A Numerical Study of Flow and Heat Transfer in a Smooth and Ribbed U-Duct with and Without Rotation," *Journal of Heat Transfer*, Vol. 123, April 2001, pp. 219–232.

[15]Iacovides, H., Launder, B. E., and Li, H.-Y., "The Computation of Flow Development through Stationary and Rotating U-Ducts of Strong Curvature," *International Journal of Heat and Fluid Flow*, Vol. 17, No. 1, 1996, pp. 22–33.

[16]Bonhoff, B., Tomm, U., Johnson, B. V., and Jennions, I., "Heat Transfer Predictions for Rotating U-Shaped Coolant Channels with Skewed Ribs and with Smooth Walls," American Society of Mechanical Engineers, ASME Paper 97-GT-162, June 1997.

[17]Azad, G. S., Uddin, M. J., Han, J. C., Moon, H. K., and Glezer, B., "Heat Transfer in Two-Pass Rectangular Rotating Channels with 45° Parallel and Crossed Rib Turbulators," American Society of Mechanical Engineers, ASME Paper 2001-GT-0186, 2001.

[18]Al-Qahtani, M. S., Jang, Y. J., Chen, H. C., and Han, J. C., "Flow and Heat Transfer in Rotating Two-Pass Rectangular Channels (AR = 2) by Reynolds Stress Turbulence Model," *International Journal of Heat and Mass Transfer*, Vol. 45, No. 9, 2002, pp. 1823–1838.

[19]Griffith, T. S., Al-Hadhrami, L., and Han, J. C., "Heat Transfer in Rotating Rectangular Cooling Channels with Angled Ribs," *Journal of Heat Transfer*, Vol. 124, No. 4, 2002, pp. 617–625.

[20]Al-Qahtani, M. S., Chen, H. C., and Han, J. C., "A Numerical Study of Flow and Heat Transfer in Rotating Rectangular Channels (AR = 4) with 45° Rib Turbulators by Reynolds Stress Turbulence Model," American Society of Mechanical Engineers, ASME Paper GT-2002-30216, June 2001.

[21]Chen, H. C., Jang, Y. J., and Han, J. C., "Near-Wall Second-Moment Closure for Rotating Multipass Cooling Channels," *Journal of Thermophysics and Heat Transfer*, Vol. 14, No. 2, 2000, pp. 201–209.

[22]Chen, H. C., Jang, Y. J., and Han, J. C., "Computation of Heat Transfer in Rotating Two-Pass Square Channels by a Second-Moment Closure Model," *International Journal of Heat and Mass Transfer*, Vol. 43, No. 9, 2000, pp. 1603–1616.

[23]Chen, H. C., Patel, V. C., and Ju, S., "Solutions of Reynolds-Averaged Navier–Stokes Equations for Three-Dimensional Incompressible Flows," *Journal of Computational Physics*, Vol. 88, No. 2, 1990, pp. 305–336.

[24]Chen, H. C., and Patel, V. C., "The Flow Around Wing-Body Junctions," *Proceedings of the 4th Symposium on Numerical and Physical Aspects of Aerodynamic Flows*, edited by T. Cebeci, California State Univ., Long Beach, CA, 1989.

[25]Chen, H. C., and Chen, M., "Chimera RANS Simulation of a Berthing DDG-51 Ship in Translational and Rotational Motions," *International Journal of Offshore and Polar Engineering*, Vol. 8, No. 3, 1998, pp. 182–191.

[26]*GRIDGEN User Manual*, Ver. 13.3, Pointwise Inc., Bedford, TX, 1999.

[27]Rohsenow, W. M., and Choi, H., *Heat, Mass and Momentum Transfer,* Prentice–Hall, Englewood Cliffs, NJ, 1961, pp. 192, 193.

[28]Kays, W. M., and Crawford, M. E., *Convective Heat and Mass Transfer*, Third ed., McGraw–Hill, New York, 1993, pp. 249, 250.